CrossMark

Multi-directional wave spectra from marine X-band radar

Björn Lund[1] · Clarence O. Collins III[2] · Hitoshi Tamura[3] · Hans C. Graber[1]

Abstract The signal measured by heave–pitch–roll directional wave buoys yields the first four coefficients of a Fourier series. Data adaptive methods must be employed to estimate a directional wave spectrum. Marine X-band radars (MRs) have the advantage over buoys that they can measure "model-free" two-dimensional (2D) wave spectra. This study presents the first comprehensive validation of MR-derived multi-directional wave characteristics. It is based on wave data from the 2010 Impact of Typhoons on the Ocean in the Pacific (ITOP) experiment in the Philippine Sea, namely MR measurements from R/V *Roger Revelle*, Extreme Air–Sea Interaction (EASI) buoy measurements, as well as WAVEWATCH-III (WW3) modeling results. Buoy measurements of mean direction and spreading as function of frequency, which do not require data adaptive methods, are used to validate the WW3 wave spectra. An advanced MR wave retrieval technique is introduced that addresses various shortcomings of existing methods.

Spectral partitioning techniques, applied to MR and WW3 results, reveal that multimodal seas are frequently present. Both data sets are in excellent agreement, tracking the evolution of up to 4 simultaneous wave systems over extended time periods. This study demonstrates MR's and WW3's strength at measuring and predicting 2D wave spectra in swell-dominated seas.

✉ Björn Lund
blund@rsmas.miami.edu

1   Rosenstiel School of Marine and Atmospheric Science, University of Miami, 4600 Rickenbacker Causeway, Miami, FL 33149, USA

2   Naval Research Laboratory, Stennis Space Center, MS, USA

3   Port and Airport Research Institute, Yokosuka, Japan

1 Introduction

Surface wave directionality is important for the prediction of swell, nonlinear wave–wave interactions, and dissipation. It is also believed to play a critical role in the formation of extreme waves (e.g., Tamura et al. 2009). Heave–pitch–roll buoy data yield four directional parameters per frequency: mean direction, spreading, skewness, and kurtosis (Kuik et al. 1988). To estimate the full two-dimensional (2D) wave spectrum, it is common practice to employ a parametric model (e.g., the $\cos^{2s}$ model (Longuet-Higgins et al. 1963) or a data-adaptive method (e.g., the maximum likelihood method (Capon et al. 1967) or the maximum entropy method (Lygre and Krogstad 1986)). The former are typically limited to unimodal seas, the latter cannot resolve more than bimodal seas at each frequency (e.g., Ewans 1998). The result will always be subjective, i.e., it varies depending on the transform method employed. Marine X-band radars (MRs) have the advantage over single-point heave–pitch–roll buoys that they operate in time and space. Hence, their measurements of the microwave return from

the sea surface can be analyzed to yield "model-free" 2D wave spectra that are capable of resolving multimodal seas.

Third-generation (3G) wave models, such as WAVEWATCH-III (WW3), have good skill in predicting peak and integrated wave parameters, including peak and mean wave direction. But their ability to accurately predict the directional distribution of wave energy is still under debate (Rogers and Wang 2006, and references therein). This is partially due to the limited availability of accurate fully-directional wave measurements. For example, in order to avoid data-adaptive methods, Rogers and Wang (2007) limited their buoy-based validation of WW3's directional prediction capabilities to the mean direction and spreading. The validation of 2D wave measurements in a meaningful, compact manner is also difficult. Khandekar et al. (1994) comparison of 2D spectra from a 3G wave model and a buoy is limited by its qualitative nature. Similarly, Krogstad et al. (1999) provide only qualitative side-by-side comparisons of 2D spectra from a high-frequency (HF) radar and a buoy (using both a data-adaptive and a parametric model) for four instances in time.

MRs could potentially meet the need for easily accessible, accurate multi-directional wave data. But, judging by the small number of publications on this topic, they have not yet been fully embraced by the wave science community. The few existing studies focus on validating MR-derived peak and integrated wave parameters as well as frequency spectra (Nieto Borge et al. 1999, 2004; Izquierdo et al. 2004; Hessner et al. 2008). One notable exception is Nieto Borge and Guedes Soares's (2000) analysis of directional wave characteristics from MR and buoy measurements, but they provide only one comparison of mean wave direction, spreading, and 2D wave spectra. Similarly, Ludeno et al. (2014) compare 2D wave spectra from shipboard MR and WW3 only qualitatively. Wyatt et al. (2003) perform more extensive side-by-side comparisons of 2D wave spectra from a MR, an HF radar, a buoy, and a 3G wave model, covering six instances of time. However, results are inconclusive, showing significant discrepancies between the different sources of wave data.

This study's goal is to conclusively establish MR's ability to accurately measure multi-directional wave spectra. To this end, an advanced wave retrieval technique is proposed that (1) accounts for near-surface vertical current shear, (2) removes background noise contributions from the wave results, (3) minimizes the wave results' dependency on the analysis windows' range and orientation, and (4) ensures a shipboard performance that is equivalent to that of fixed coastal stations. This study draws from shipboard MR measurements, Extreme Air–Sea Interaction (EASI) wave buoy data, and WW3 model results that were acquired during the 2010 Impact of Typhoons on the Ocean in the Pacific (ITOP) field experiment in the Philippine Sea. It covers a

much larger amount of data than previous MR directional wave retrieval studies. Its focus lies on the waves' directional characteristics, i.e., differences in the frequency distribution of the wave energy will be noted but not addressed further here.

The EASI measurements are used to validate the WW3 model results in terms of spectral parameters as well as spreading and mean wave direction as function of frequency. The non-symmetrical hull type used by EASI (based on the 6-m Navy Oceanographic Meteorological Automatic Device (NOMAD)) has in the past been considered unsuitable for directional wave retrieval (Teng 2002). But recently Collins et al. (2014) performed a wave sensor comparison that established the validity of EASI directional wave measurements. Their study includes a MR–EASI comparison, showing good agreement for the peak wave direction and period. Here, due to the limited number of coincident MR/EASI measurements, and the inherent subjectivity of buoy 2D wave spectra, the MR data are compared exclusively with the WW3 results. The EASI–WW3 comparison is used as performance benchmark. In addition to statistical and qualitative analysis methods, the study employs a fully automated partitioning method to track wind sea and swell systems within the MR and WW3 2D wave spectra.

This paper is organized as follows: Section 2 describes the ITOP experiment and provides a data overview. Section 3 briefly revisits the standard MR wave retrieval technique and introduces the advancements that were implemented. The multi-directional wave results from EASI, WW3, and MR are presented in Section 4. The paper ends with concluding remarks and suggestions for future research (Section 5).

2 Data overview: ITOP experiment

The goal of the 2010 ITOP field experiment in the Philippine Sea was to study the impact of tropical cyclones (TCs) on the Pacific Ocean. Sponsored by the US Office of Naval Research (ONR), ITOP involved several national and international research institutions and included remote sensing, modeling, as well as in situ measurement activities. The latter comprised meteorological and oceanographic observations from airplanes, research vessels, drifters, and moorings (D'Asaro et al. 2014). This study combines MR remote sensing, EASI buoy measurements, and WW3 modeling results.

A science MR system was installed on the main mast of R/V *Roger Revelle* at a height of ∼19 m above water level. It was connected to a Wave Monitoring System (WaMoS), which consists of a personal computer with a radar data acquisition board, hard drives for storage, and a software package to produce operational wave and current results

Table 1 Technical specifications of the science MR system on the *Revelle*

| MR/WaMoS parameter	Value
Antenna height	∼19 m
Wavelength	∼3 cm
Polarization	HH
Antenna rotation period	∼1.4 s
Horizontal antenna beam width	0.75°
Range resolution	10.5 m
WaMoS range cell size	7.5 m
WaMoS azimuth cell size	∼0.3°
WaMoS range	248–2,153 m

(Dittmer 1995; Ziemer 1995). The radar operates at 9.4 GHz (X-band), i.e., a wavelength of ∼3 cm. Its horizontally polarized antenna has a rotation period of ∼1.4 s and a horizontal beamwidth of 0.75°. It was set to transmit at short pulse (0.07 μms), which corresponds to a range resolution of 10.5 m. WaMoS continuously sampled the radar data with cell sizes of 7.5 m in range and ∼0.3° in azimuth, covering a range of 248–2153 m. The technical specifications of the science MR system on the *Revelle* are summarized in Table 1.

The MR data used for this study stem from 4 *Revelle* cruises from Aug. to Oct. 2010 (namely, RR1010, RR1012, RR1014, and RR1015). In total, ∼26 days of MR data were collected during these cruises. Figure 1a shows the *Revelle* cruise tracks superimposed on a bathymetric map of the ITOP study area. It also includes the locations of two ASIS–EASI buoy pairs that were deployed at 21.28° N, 126.88° E (5450-m depth) and 19.68° N, 127.38° E (5500 m). At both sites, an ASIS (Air–Sea Interaction Spar) buoy was tethered to EASI, which was anchored to the seafloor (Graber et al. 2000; Drennan et al. 2014). Figure 1b shows a picture of an

ASIS–EASI buoy pair from ITOP, with the *Revelle* in the background.

Most of the ASIS buoys' wave wires failed early on in the experiment, rendering accurate wave direction measurements difficult. Hence, this study focuses exclusively on the EASI wave measurements. With its NOMAD-type hull, EASI was designed as a metocean platform that can withstand TC conditions. To measure directional wave information, the EASIs were treated as single point triplets (Longuet-Higgins et al. 1963). As shown by Collins et al. (2014), the EASI wave data collected during ITOP have an accuracy that is comparable with other more established sensors. The northern EASI buoy (EASI-N) was operational from 6 Aug. to 13 Dec. 2010 and the southern one (EASI-S) from 4 Aug. to 22 Nov. 2010. However, due to compass issues, wave directional information from EASI-S are available until 2 Nov. 2010 only. For details on the atmospheric conditions encountered by EASI-N, the reader is referred to Potter et al. (2015).

The MR and EASI wave measurements are complemented by results from a 3G wave model, WW3 version 3.14 (Tolman 2009). The model has a nested domain with grid resolutions of 0.3° for the outer nest (covering the Pacific excluding the poles) and 0.1° for the inner nest (northwestern Pacific). The hindcast covers the full year 2010 for the outer nest and the 5-month period from July through November for the inner nest. Tolman and Chalikov's (1996) source terms are used, and the discrete interaction approximation method is employed as the nonlinear transfer function (Hasselmann et al. 1985). For spatial propagation of the wave spectrum, the default third-order advection scheme is used. WW3 was forced by the 6-hourly NCEP-NCAR reanalysis surface winds (Saha et al. 2010). WW3 directional wave spectra were stored every 30 min along the *Revelle* cruise track and every 1 h at the EASI buoy locations. They have 35 frequencies ranging from 0.041 to
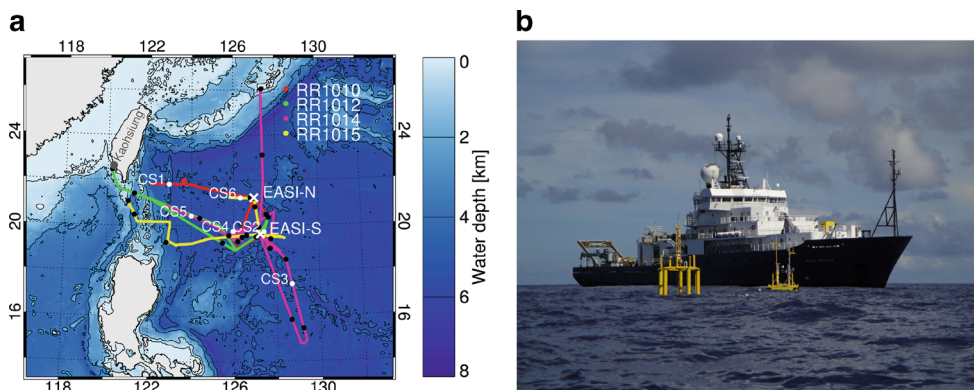
Fig. 1 a Map of R/V *Roger Revelle* cruise tracks during the ITOP experiment. Tracks are limited to the time periods for which MR data are available. A *black dot* is plotted every 24 h. The ASIS–EASI buoy positions are marked by white crosses. The *white dots* mark the ship's

locations at the times of the six case studies discussed below. The bathymetry is from the GEBCO Digital Atlas (IOC et al. 2003). **b** Picture of the *Revelle* and an ASIS–EASI buoy pair in the Philippine Sea

1.05 Hz (with a relative frequency of 10 %, $f_{m+1} = 1.1 f_m$, where f is the frequency and m a discrete grid counter) and 36 directions ($\Delta\theta = 10°$).

3 Advancements to marine radar surface wave retrieval

3.1 Standard wave retrieval

To determine 2D wave spectra, this study builds on the well-established three-dimensional (3D) analysis of MR image sequences that was first proposed by Young et al. (1985) and further developed by Senet et al. (2001) and Nieto Borge et al. (2004). In the following, this standard analysis method is briefly revisited.

The horizontally (HH) polarized, grazing incidence, X-band microwave sea return is controlled by the sea surface roughness, with Bragg scattering and small-scale wave breaking playing decisive roles (Barrick 1968; Trizna et al. 1991). Under favorable environmental conditions (i.e., wind speeds and significant wave heights greater than 3 ms^{-1} and 0.5 m, respectively), MR images of the sea surface include a long (here, >21 m) gravity wave signal, the so-called "sea clutter". The wave imaging mechanisms include hydrodynamic modulation, tilt modulation, and shadowing (Alpers et al. 1981; Wetzel 1990). These are nonlinear processes whose full understanding remains elusive (Lyzenga and Ericson 1998; Plant 2003). Figure 2 gives an MR image example showing a dominant swell from the southwest (visible as dark and bright bands at all ranges) and a wind sea from the south-southeast (visible along its propagation axis in the near range). The image was acquired from the *Revelle* on 11 Aug 2010, 0600 UTC.
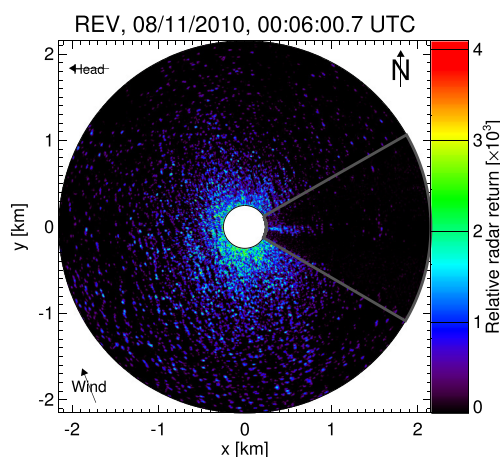
Fig. 2 Example of MR image acquired from the *Revelle* on 11 Aug 2010, 0600 UTC. The shadowed slice of the radar FOV is surrounded by a gray frame. The color scale corresponds to the relative radar return and ranges from *black* (minimal return) to *red* (maximum return)

The MR wave retrieval by Young et al. (1985), Ziemer and Dittmer (1994), Dittmer (1995), Senet et al. (2001), and Nieto Borge et al. (2004, 2008) consists of the following steps:

1. *Polar to Cartesian transform:* Sequences of rectangular analysis windows are extracted from a series of polar radar images. The analysis windows are located at a fixed range and select azimuths relative to the radar platform, e.g., windows of 256 × 128 pixels with a minimum range of 750 m and azimuths of 0°, 110°, and 250° from the ship bow.

2. *Demeaning:* The overall mean intensity is subtracted from the image sequence. This and the following steps are applied separately for each analysis window.

3. *3D Fast Fourier Transform (FFT):* A 3D FFT is employed to convert the radar image sequence to wavenumber frequency space. In the resulting 3D image spectrum, the surface wave energy is located on the so-called dispersion shell, defined by the linear dispersion relationship $\varsigma = \pm\sqrt{gk \tanh kh} + \mathbf{k}\cdot\mathbf{U}$. Here, ς is the intrinsic frequency, $k = |\mathbf{k}|$ the wavenumber, g the acceleration due to gravity, h the water depth, and $\mathbf{U}$ the encounter current velocity (i.e., ship motion and near-surface current combined).

4. *Encounter current velocity fit:* To determine the near-surface current, spectral coordinates with power above some threshold are attributed to the surface waves. The best-guess current velocity is obtained through an iterative least-squares fit that minimizes the spectral coordinates' distance from the dispersion shell. Frequencies below a certain cut-off frequency are disregarded.

5. *Dispersion filter:* Spectral energy outside of the Doppler-shifted dispersion shell (the so-called background noise) is set to zero. This step removes most background noise from the 3D image spectrum.

6. *Modulation transfer function (MTF):* The MTF converts the radar image spectrum to an ocean wave spectrum. Differences between the two are due to the radar imaging mechanisms. Uncertainties regarding these mechanisms place limitations on determining the MTF. Nonetheless, from a combination of in situ measurements and numerical simulations, Nieto Borge et al. (2004) found the MTF $|\mathcal{M}(k)|^2 = F_r(k)/F_w(k)$ to be proportional to $k^{1.2}$. Here, F_r is the radar image spectrum and F_w the ocean wavenumber one. After application of the MTF, the 2D ocean wavenumber spectrum is obtained by frequency integration. With the help of the linear dispersion relationship, it can easily be transformed to the more commonly used frequency direction spectrum.

7. *Signal-to-noise ratio (SNR):* The square root of the SNR (i.e., the ratio between the spectral energy attributed to

the waves and the background noise) correlates linearly with the significant wave height H_s. The correlation parameters need to be determined for each MR installation with the help of reference H_s measurements.

For a complete review of the standard MR wave retrieval method, readers are referred to Lund et al. (2014).

3.2 Advanced wave retrieval

The MR results presented in this study were obtained using an advanced wave (and near-surface current) retrieval algorithm. This algorithm is based on the standard method outlined in the previous subsection, but incorporates several advancements, most of which were developed in the context of shipboard MR near-surface current and bathymetry retrieval.

Several recent studies point towards issues with MR wave results that were obtained using the standard method. Stredulinsky and Thornhill (2011) found that peak wave directions θ_p and periods T_p from shipboard MR are good, whereas H_s estimates are unreliable. Working on a different MR data set, Cifuentes-Lorenzen et al. (2013) came to the same conclusion, noting that results deteriorate for ship speeds (over ground) $>3 \text{ ms}^{-1}$. Lastly, Lund et al. (2014) demonstrated that the MR wave results depend on the analysis windows' orientation and range, which negatively affects shipboard measurements in particular.

These issues can be explained, at least partially, by shortcomings within the standard retrieval method. Some of these shortcomings have been addressed in recent works, albeit mostly in the context of bathymetry and near-surface current retrieval:

– *Georeferencing:* The standard method's platform-based coordinate frame requires the (generally false) assumption of a constant ship velocity throughout the analysis period (typically, ~1–2 min). In order to allow for course changes during the analysis period and reduce aliasing issues, shipboard radar data need to be georeferenced (Bell and Osler 2011; Lund et al. 2015b).
– *Trilinear interpolation:* The standard method furthermore assumes that ship and sea surface are static during the time needed for one radar sweep. This snapshot simplification can be done away with by employing a pulse-resolved, trilinear (i.e., in space and time) interpolation when transforming the raw polar radar data to a Cartesian grid (Lund et al. 2015b).
– *Range and azimuth dependency:* To remove biases towards waves traveling along the line of sight between radar and analysis window, Al-Habashneh et al. (2015) proposed an algorithm that recursively adjusts the analysis window orientation to best match the given wave

state. Lund et al. (2015b) opted to analyze the whole radar field of view (FOV). This approach requires a homogeneous wave and current field within the radar footprint, a condition that is generally satisfied in the open ocean.
– *Auxiliary heading sensor and near-surface current "calibration":* The need for accurate ship heading measurements was first discussed by Bell and Osler (2011). They observed jittering targets within their radar image sequences, which compromise an accurate bathymetry retrieval. To reduce the jitter, they proposed a cross-correlation-based image analysis technique. Lund et al. (2015a) demonstrated that even small ($<1°$) inaccuracies in the heading measurement or image misalignments introduce significant errors in the radar-derived near-surface currents. They suggest that, as for shipboard ADCP measurements (Firing and Hummon 2010), heading sensors must provide O ($0.1°$) accuracy. Furthermore, they propose a near-surface current "calibration" method to identify and remove fixed radar image misalignments.
– *Near-surface vertical current shear:* The near-surface currents sensed by MR represent depth-weighted averages (Stewart and Joy 1974). The longer the waves on which the current estimate is based, the greater its "effective" depth. Lund et al. (2015b) exploited this relationship and proposed a wavenumber-dependent current fit that yields multiple independent current estimates corresponding to effective depths from ~2–8 m. This stands in contrast to the standard method, which treats all wavenumbers in bulk, yielding a single current vector per measurement period.

The MR wave retrieval method implemented here builds on the near-surface current "calibration" and vertical current shear retrieval methods described by Lund et al. (2015a, b). These studies use the same ITOP data set as here. They show excellent agreement between the shipboard MR and ADCP current measurements as well as shear results that are in accord with physical expectations. The link between MR near-surface current and wave retrieval is obvious, since the latter is an integral part of the former (see previous subsection). The interested reader is referred to Lund et al. (2015b) for further details on the current retrieval methodology employed here. Several further improvements were made to the standard wave retrieval method, which will be described in the following.

The standard method solely uses the dispersion filter to remove background noise from the 3D image spectrum. Noise that is located on the dispersion shell is interpreted as a wave signal. Lund et al. (2015b) introduced a novel empirical method to determine the spectral characteristics of the background noise. They show that it decays rapidly
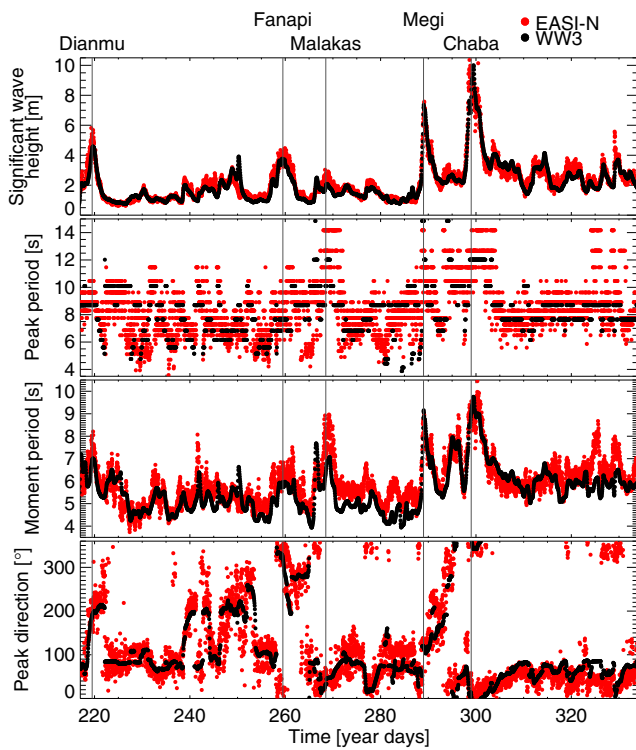
Fig. 3 Time series of spectral wave parameters measured by EASI-N (*red*) and corresponding WW3 modeling results (*black*). The plot includes all ~117 days of concurrent EASI-N and WW3 data. The *vertical bars* mark the passage of the 5 TCs encountered by EASI-N

inaccuracies in determining the background noise characteristics, only spectral points with a SNR greater than 1.2 are retained.

Finally, the standard method assumes the near-surface current to be wavenumber-invariant. As shown by Lund et al. (2015b), and argued above, this is a false assumption. Hence, this study uses a dispersion filter that accounts for near-surface vertical current shear. This maximizes the energy attributed to waves, especially for the relatively short waves which experience the strongest current-induced Doppler shift.

4 Multi-directional wave results

4.1 WW3 model validation: comparison with EASI measurements

The following comparison between WW3 wave model results and EASI wave measurements has the dual purpose of validating WW3 and providing a benchmark for the subsequent WW3–MR comparison. The focus of this study lies on the directional wave characteristics. WW3 directly calculates the 2D wave spectrum $E(f, \theta)$. Buoy wave measurements permit only an approximation of $E(f, \theta)$, via the first four Fourier coefficients $[a_1(f), b_1(f), a_2(f), b_2(f)]$. Following Rogers and Wang (2007), this study avoids data adaptive methods because they are subjective. Instead, EASI buoy directional wave measurements are presented as given, i.e., through the mean direction θ_m and directional spreading σ_θ. Both parameters can be directly inferred from a heave–pitch–roll buoy time series (Kuik et al. 1988):

$$\theta_m(f) = \arctan\left(\frac{b_1(f)}{a_1(f)}\right), \tag{1}$$

$$\sigma_\theta(f) = \sqrt{2[1 - m_1(f)]}, \tag{2}$$

$$m_1(f) = \sqrt{a_1(f)^2 + b_1(f)^2}. \tag{3}$$

with increasing wavenumber and frequency. Furthermore, if the 3D Fourier analysis is carried out over the whole radar FOV, the background noise becomes azimuthally independent. [Note that a portion of the radar FOV (surrounded by a gray frame in Fig. 2) is shadowed by ship superstructures.] Here, this knowledge is employed to completely remove the background noise from the wave results. This is done by determining the 2D background noise spectrum via frequency integration, in the same manner as the 2D wave spectrum is obtained. The background noise can then simply be subtracted from the wave spectrum. To account for small

Table 2 EASI and WW3 spectral wave parameter comparison statistics (with RMSE being the root-mean-square error and N the number of data pairs)

	WW3–EASI-N				WW3–EASI-S			
	H_s	T_p	T_{m01}	θ_p	H_s	T_p	T_{m01}	θ_p
r, R	0.94	0.53	0.81	0.80	0.94	0.61	0.86	0.76
Bias	−0.09 m	−0.35 s	−0.36 s	−0.4°	−0.16 m	−0.28 s	−0.37 s	−2.5°
RMSE	0.45 m	1.91 s	0.71 s	41.5°	0.49 m	1.74 s	0.68 s	46.6°
σ_{xy}	0.44 m	1.88 s	0.61 s	41.5°	0.46 m	1.71 s	0.58 s	46.6°
N	2809	2809	2809	2809	2641	2641	2641	2175

Fig. 4 **a** EASI-N mean direction as function of frequency and time. **b** Corresponding WW3 result
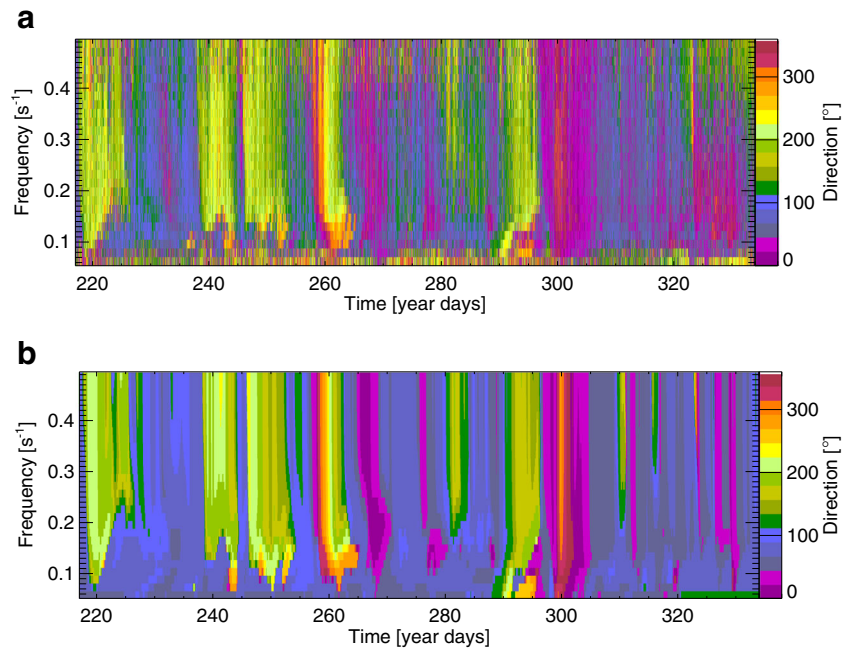

The same quantities can be computed from the $E(f, \theta)$ output by WW3 with

$$a_1(f) + ib_1(f) = \frac{1}{\pi} \int_0^{2\pi} \exp(i\theta) E(f, \theta) d\theta. \quad (4)$$

To add meaning to this study of directional wave characteristics, it is first shown that spectral parameters are well predicted by WW3. Figure 3 gives a time series of the significant wave height H_s, peak wave period T_p, first moment period T_{m01}, and peak wave direction θ_p from EASI-N and WW3. The time series covers the entire period over which data from both buoy and model are available (i.e., $\sim$117 days of data, with each data pair being 1 h apart). Both buoy and model document the passage of five TCs, namely Tropical Storm Dianmu [year day (YD) $\sim$219.5], Typhoon Fanapi (YD $\sim$259.5), Typhoon Malakas (YD $\sim$268.5), Super Typhoon Megi (YD $\sim$289), and Typhoon Chaba (YD $\sim$299). EASI-N recorded its maximum H_s of 10.9 m and maximum 30-min sustained winds (not plotted)

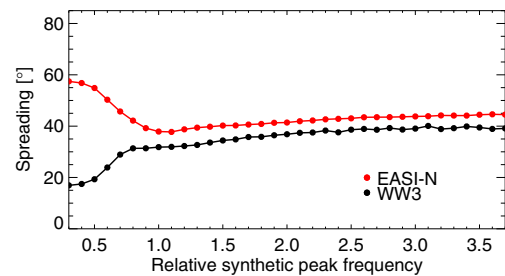**Fig. 5** **a** EASI-N directional spreading as function of frequency and time. **b** Corresponding WW3 result
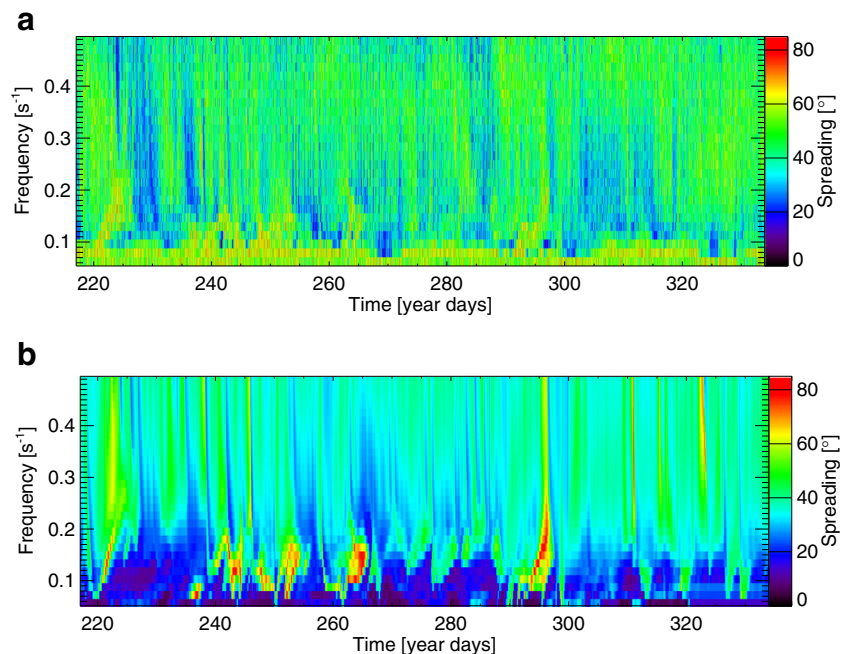
of 26 m s^{-1} during Chaba (Collins et al. 2014; Potter et al. 2015). WW3's T_{m01} was determined over the same range of frequencies as covered by EASI. It is biased low, indicating that the model overestimates the high-frequency wave energy. Alternatively, the bias could be due to EASI's 6-m hull, which likely reduces the buoy's sensitivity to short waves. But overall, the peak and integrated wave parameters are in good agreement.

This is confirmed by the comparison statistics shown in Table 2. The EASI-S measurements and corresponding WW3 results (∼110 days of coincident data) are not shown here, nor in the following, but they compare equally well, as indicated by the statistics in Table 2.[1] The relatively low correlation coefficients r and high standard deviations σ_{xy} observed for the T_p comparisons are partly due to the discrete nature of the parameter (the resolution becomes coarser with increasing wave period), and partly due to the presence of multiple wave systems with similar energy but different peak frequencies. The intercomparison of wave measurements from the same experiment, conducted by Collins et al. (2014), yielded only slightly better comparison statistics. All this suggests that WW3 performed well within the ITOP study area and period. (The EASI and model winds, not shown here, are in good agreement. For wind speed, referenced to 10 m height, and wind direction, the correlation coefficient and mean directional difference length are 0.85 and 0.91 with standard deviations of 2.08 m s^{-1} and 27.9° and biases of −0.63 m s^{-1} and 1.9°, respectively.)

Figure 4a, b illustrates the mean direction as function of frequency and time for EASI-N and WW3, respectively. The WW3 mean direction was linearly interpolated to match the EASI-N frequency range and resolution. Both figures cover the full study period. It is evident that observations and model are in good qualitative agreement. The observations exhibit a significant degree of scatter, which may be explained by sampling variability (Krogstad et al. 1999). The scatter is especially pronounced at the low frequencies. Both EASI-N and WW3 show a dominant mean direction from northeast to southeast at all frequencies. These "background" wave conditions are frequently disturbed by storm events. During all five TCs recorded by EASI-N and modeled by WW3, the mean direction changes significantly and exhibits an enhanced variability over frequency. This variability indicates the presence of multiple wave systems, which is to be expected in TC vicinity (Holthuijsen et al. 2012).

_____

[1] Note that for θ_p the mean directional difference length R is used to measure the degree of correlation. It is defined as the length of the vector mean of the set of unit vectors, each of which is oriented by the difference in angles between the two series; a value of 1 means perfect correlation and 0 means no correlation at all.

Fig. 6 Temporally averaged directional spreading as function of relative synthetic peak frequency for EASI-N (*red*) and WW3 (*black*). Data shown correspond to the ∼117 days of EASI-N operation and WW3 availability

Figure 5a, b shows the frequency-time dependency for the EASI-N and WW3 directional spreading. Again, the WW3 spreading was interpolated over frequency to match EASI-N. For wind seas, it is well known that directional spreading is most narrow at the peak frequency and broadens on either side of it (Rogers and Wang 2007). At the EASI buoy locations in the Philippine Sea, seas are generally mixed with an important swell component. This makes it more difficult to interpret the spreading reported here. Nevertheless, the figures allow the following observations. The qualitative agreement is not as good as for the mean
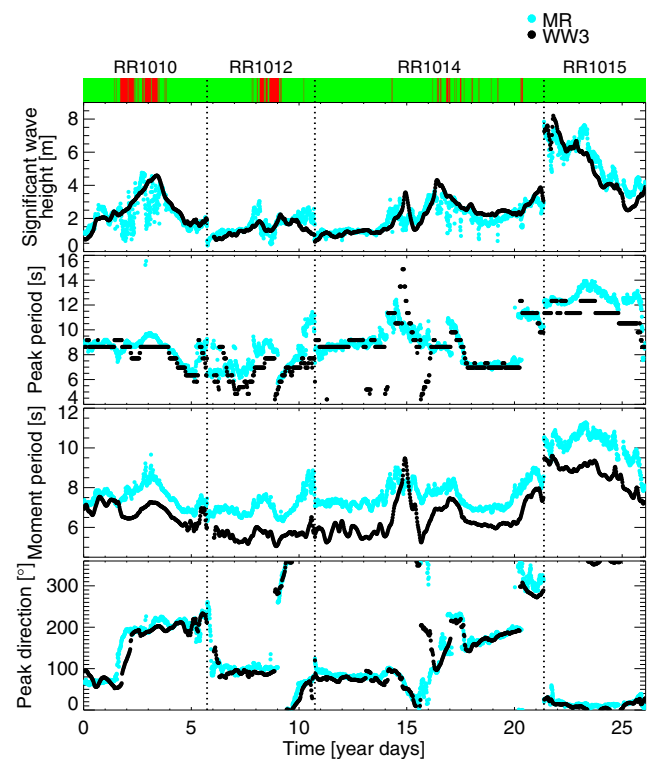
Fig. 7 Time series of spectral wave parameters along the *Revelle* track as measured by MR (*cyan*) and modeled using WW3 (*black*). The *horizontal bar on top* marks periods of heavy rain in *red*. The plot covers all four cruises, corresponding to ∼26 days of data

**Table 3** MR and WW3 spectral wave parameter comparison statistics

	WW3–MR			
	H_s	T_p	T_{m01}	θ_p
r, R	0.91	0.81	0.89	0.90
Bias	0.00 m	−0.62 s	−1.18 s	−8.2°
RMSE	0.65 m	1.38 s	1.29 s	32.0°
σ_{xy}	0.65 m	1.23 s	0.54 s	31.0°
N	1224	1224	1224	1224

wave direction. Differences are especially pronounced at frequencies <0.1 s^{-1}, with WW3 directional spreading much narrower than the observations. The EASI-N directional spreading has large scatter at all frequencies, which makes it challenging to characterize. WW3 reproduces the more prominent features observed by EASI-N. For example, buoy-measured episodes of relatively broad (or narrow) seas are generally matched by WW3. Also, disregarding frequencies <0.1 s^{-1}, WW3 roughly reproduces the observed frequency dependency of the directional spreading.

To further investigate the frequency-wise variation of directional spreading, results are reorganized relative to the peak frequency. In order to avoid the large uncertainty associated with T_p, a synthetic peak period is chosen as reference. As proposed by Rogers and Wang (2007), it is defined by simple linear regression between (the much more stable) T_{m01} and T_p. Figure 6 shows the temporally

averaged directional spreading as a function of relative frequency f/f_p (where f_p is synthetic) for EASI-N and WW3. The mean EASI-N directional spreading has its minimum at the peak. The directional spreading increases rapidly below the peak frequency and more slowly with increasing frequency. At frequencies above the peak, the WW3 directional spreading also increases continuously. It is narrower by ∼5° but otherwise closely follows the EASI-N observations. Below the peak, however, the modeled directional spreading keeps decreasing, in stark contrast with the measurements. Rogers and Wang (2007) found a similar model–data misfit, although not quite as pronounced. Low-frequency wave measurements by heave–pitch–roll buoys are problematic due to the relatively weak accelerations and rates of rotation the buoys experience at these frequencies. Kuik et al. (1988) demonstrated that noise in the low-frequency wave signal positively biases the directional spreading. The large

Fig. 8 **a** MR mean direction as function of frequency and time. The four *Revelle* cruises are labeled and separated by *vertical lines*. The *horizontal bar on top* marks periods of heavy rain in *red*. **b** Corresponding mean direction from WW3
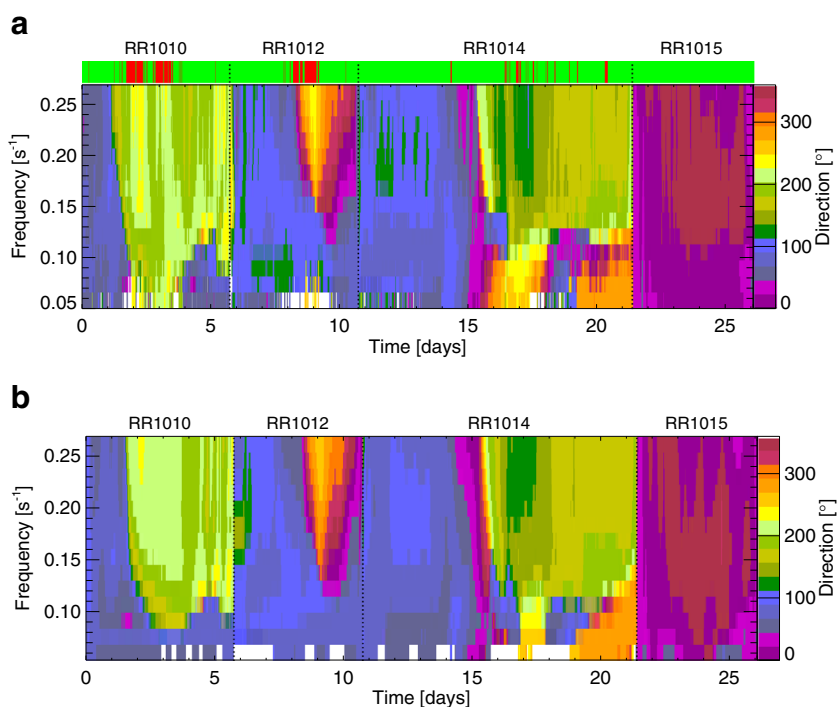
amount of scatter in the EASI-N low-frequency mean direction (see Fig. 4) suggests that buoy sensitivity issues could indeed be responsible for these discrepancies.

Despite some EASI–WW3 differences, the overall agreement between model and measurements is good. This finding paves the way for the following subsections, where WW3 results are used to establish MR's strength at measuring multi-directional wave characteristics.

4.2 MR–WW3 comparison of wave parameters

The MR wave retrieval is based on the spatio-temporal analysis of radar backscatter intensity measurements. It therefore directly yields 2D wave spectra, without data adaptive methods. Hence, the MR mean direction and directional spreading must be determined by first computing the Fourier coefficients, as for WW3 (see Eq. 4).

Figure 7 shows a time series of the MR and WW3 spectral wave parameters along the *Revelle* track on all four cruises (i.e., ∼26 days of data). Each MR data point corresponds to ∼10 min of measurements (vs. 30 min for the EASI results in the previous subsection). The four cruises were subject to winds and waves from TCs Dianmu, Fanapi, Megi, and Chaba, respectively. As observed for the EASI–WW3 comparison, the WW3 T_{m0} is biased low. But here the bias is more pronounced and cannot be explained by model prediction errors alone. It is most likely due to imperfections in the MTF that transforms the MR image spectrum into a wave spectrum (see Section 3.1). Specifically, Nieto Borge

et al.'s (2004) MTF, applied to image spectra obtained using the methodology outlined in Section 3.2, yields wave spectra that overestimate energy around the spectral peak and underestimate energy at the higher frequencies. Since this study focuses on the directional wave characteristics, which are MTF-independent (e.g., Young et al. 1985), improving the MTF is deferred to future work.

Other than this, MR and WW3 results are in good agreement, as confirmed by the corresponding comparison statistics shown in Table 3. Note that, with the exception of H_s, the MR–WW3 comparison has higher r (or R) values and lower σ_{xy} than either EASI–WW3 comparison (compare Table 2). While the MR H_s correlates well with WW3, it must be noted that the WW3 H_s was used to determine the linear calibration coefficients needed to convert the MR $\sqrt{\text{SNR}}$ to H_s (see Section 3.1). Gangeskar (2014) has shown that wave-induced geometric shadowing may yield H_s without calibration. This will be explored further in future work. Finally, note that the presence of rain negatively affects MR wave results, especially H_s estimates. While the comparison statistics in Table 3 include all data, Fig. 7 does mark occurrences of rain. Rain was identified using the radar images' zero-pixel percentage (Lund et al. 2012).

Figure 8a, b shows the MR and WW3 mean direction as function of frequency and time, covering all four *Revelle* cruises. The WW3 results were linearly interpolated over frequency to match the MR grid. The agreement is good, with the MR mean direction exhibiting much less scatter than observed in the EASI data (see Section 4). The mean

Fig. 9 **a** MR directional spreading as function of frequency and time. The four *Revelle* cruises are labeled and separated by *vertical lines*. The *horizontal bar on top* marks periods of heavy rain in red. **b** Corresponding spreading from WW3
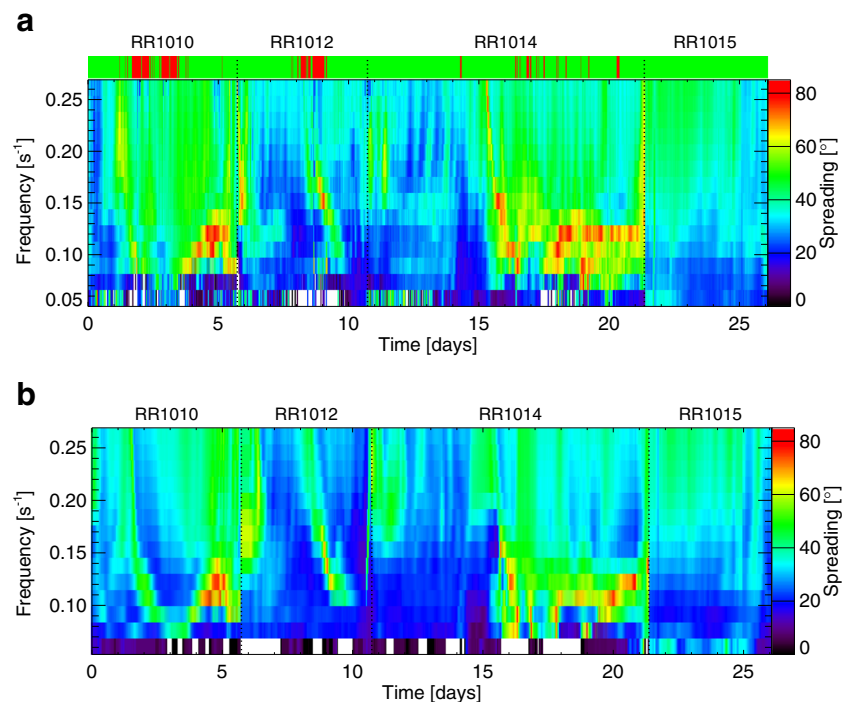
direction is highly variable both in time and frequency. This is due to the swell generated by the TCs. The ship's constantly changing position further enhances the observations' temporal variability.

Figure 9a, b depicts the corresponding MR and WW3 directional spreading. Despite the swell-dominated seas, which present a challenge to WW3 (or any wave model), the remotely-sensed and modeled results are in good agreement. The model reproduces all the distinctive features that are visible in the MR observations. As already observed for the mean direction, the MR directional spreading shows much less scatter than the EASI one. Furthermore, it is noteworthy that both MR and WW3 report a narrowing spreading at the very low frequencies. Figure 10 shows the temporally averaged MR and WW3 directional spreading as function of f/f_p (where, again, f_p is synthetic). For above-peak frequencies, WW3 underpredicts the MR spreading by $\sim5°$, as already observed in the EASI–WW3 comparison. Below the peak, both the MR and WW3 spreading briefly broaden but then narrow to minima between ~20 and $30°$ at relative synthetic peak frequencies <0.5. This is unlike the EASI observations, which have their broadest mean spreading of $\sim60°$ at the lowest relative frequency (see Section 4). This discrepancy has two possible explanations. Either MR and WW3 lack the sensitivity to resolve such low-frequency waves, or, as suggested above, the broad spreading observed by EASI is due to measurement noise rather than the sea state. The data presented here do not allow a conclusive answer.

4.3 MR–WW3 spectral partitioning and wave system tracking

To further investigate directional wave characteristics, the MR and WW3 2D spectra were partitioned into wave systems following Hanson and Phillips (2001). The wind sea corresponds to the wave partition (or partitions) whose peak meets the criteria $U_{10N}\cos\theta_d > 0.83c_p$ (Donelan et al. 1985) and $|\theta_d| < 45°$. Here, θ_d is the angle between the wind and wave direction, c_p is the phase speed, and U_{10N} is
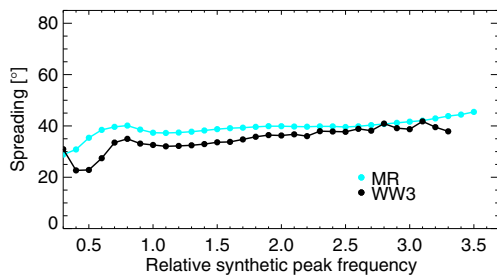
Fig. 10 Temporally averaged directional spreading as function of relative synthetic peak frequency for MR (*cyan*) and WW3 (*black*). The data shown include all four *Revelle* cruises
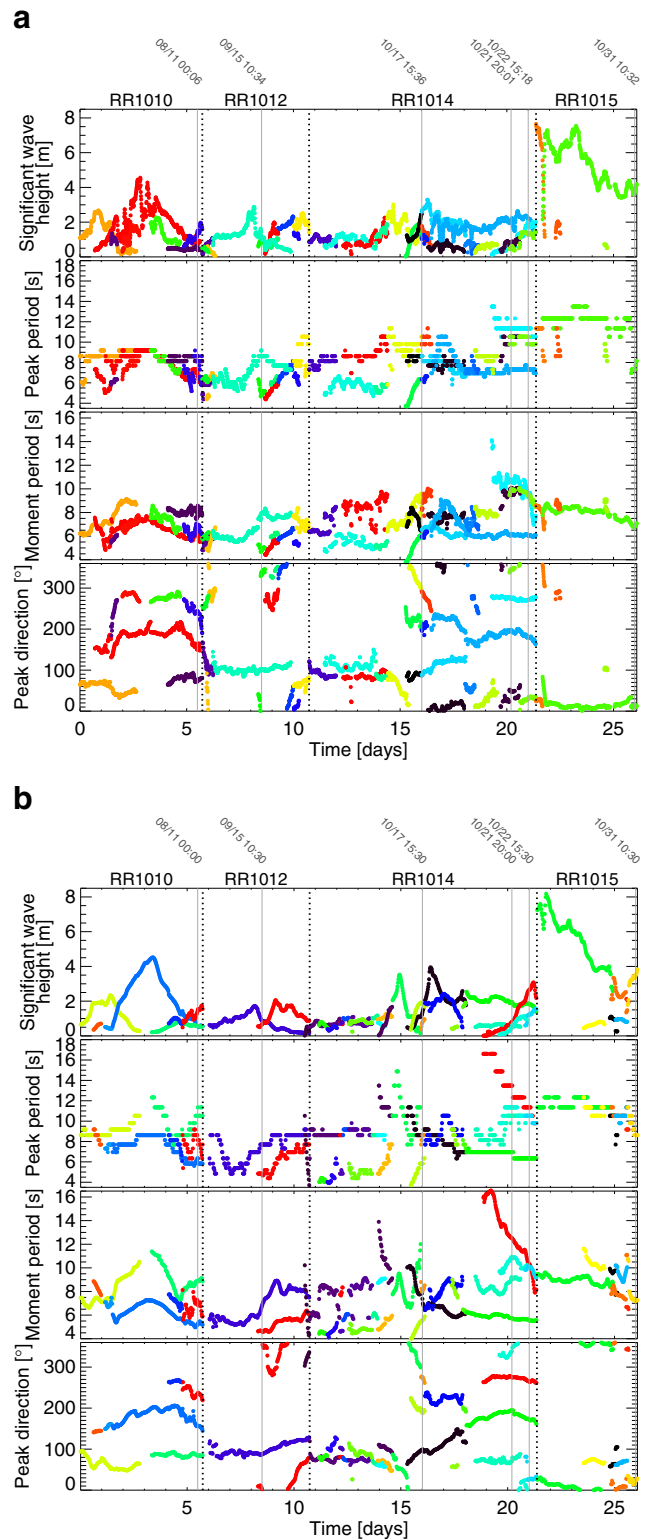

Fig. 11 MR (**a**) and WW3 (**b**) time series of spectral parameters along the *Revelle* track, determined separately for all wave systems. Each wave system was tracked over time and assigned a unique color. To facilitate distinguishing between wave systems, colors were assigned randomly. Wave systems whose partial H_s never exceeds 0.5 m are not shown. The plot covers all four cruises. Case study times are marked by *gray bars*

the 10-m neutral wind speed. During the study period, the swell is generally far more energetic than the wind sea in both measurements and model. Figure 11 shows time series of the MR and WW3 spectral parameters for each wave system, covering all four cruises. The MR and WW3 results show multimodal seas at most times. They are in good agreement, despite the swell prevalence. Over one period of several hours (on day 20), both MR and WW3 spectra show four distinct wave systems.

Figure 12 gives side-by-side comparisons of select MR and WW3 2D wave spectra. The vertical bars in Fig. 11 indicate the times of these case studies. The geographic locations are marked in Fig. 1. Each wave system is surrounded by a color-coded frame (red corresponding to the most and black to the least energetic system). The spectral coordinates inside the gray dashed line meet the above wind sea criteria. As could be expected from the time series, the spectra are in excellent agreement. Figure 12a shows

Fig. 12 Select MR and WW3 directional wave spectra for case studies. The color scale is logarithmic. The spectral coordinates that are surrounded by a *gray dashed line* are forced by the local wind. They are centered around the wind direction, marked by a *short gray bar*. Each wave system is surrounded by a frame. The frames' colors are determined by each system's partial H_s, with black corresponding to the least energetic system and red to the most energetic one. Each plot title gives date, time, and wind speed (U_{10N}). The MR spectra also give the zero-pixel percentage, with values under 50 % indicating the presence of rain
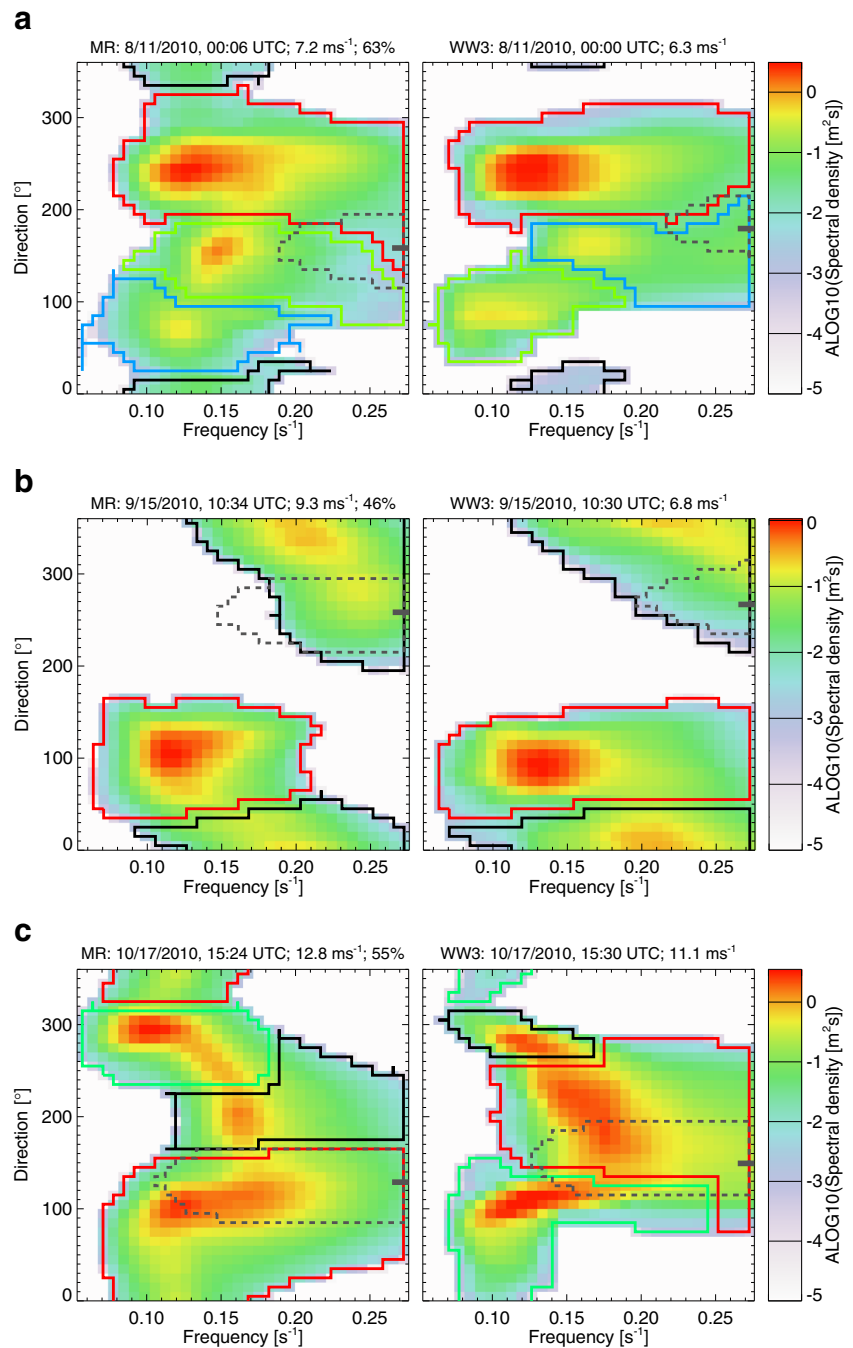
Fig. 12   (continued)
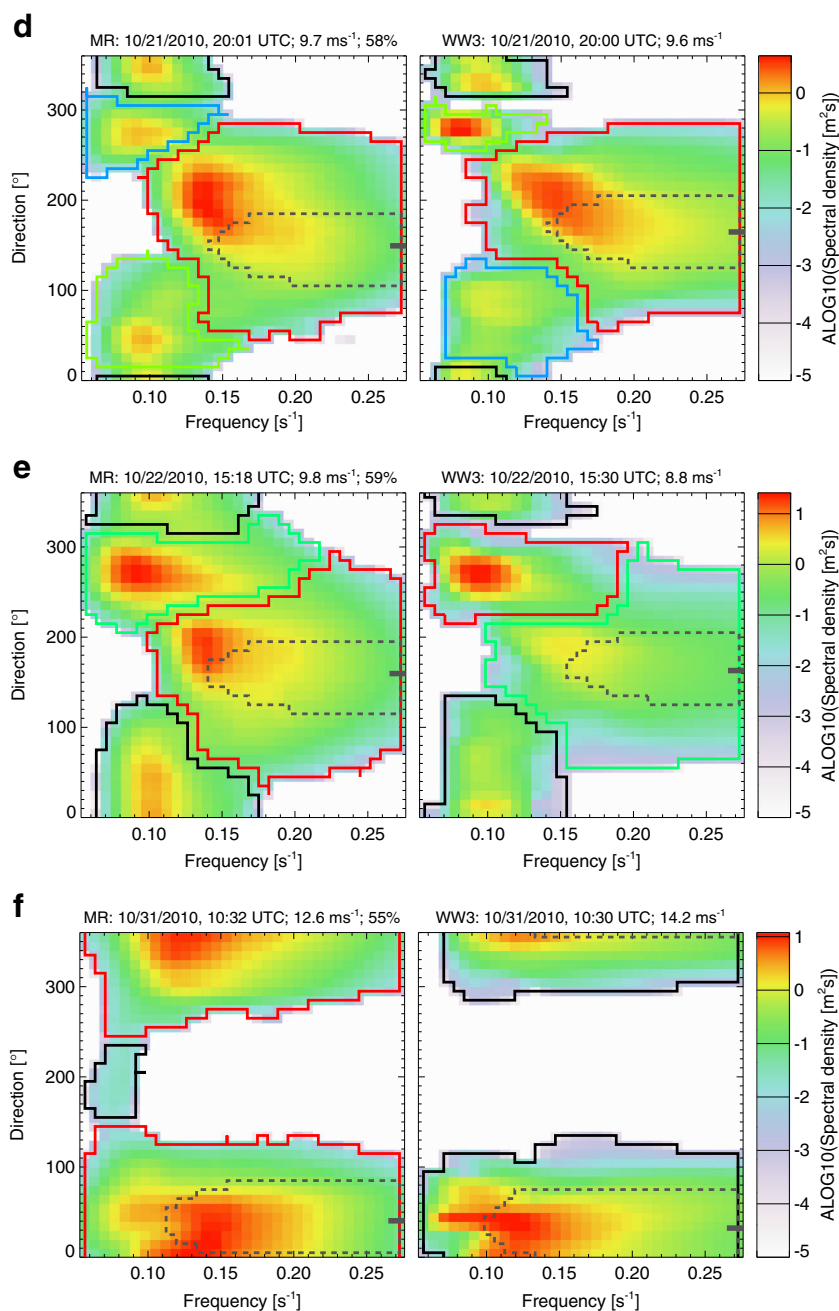
the presence of four wave systems in both measurements and model. None of the systems has its peak inside the parabolic area that is forced by the local wind. The most energetic swell system comes from the southwest, the least energetic one from the north (The latter does not show in Fig. 11 because it never exceeds the 0.5 m partial H_s threshold.). One difference is that the energetic order of the secondary and tertiary system is reversed between MR and WW3. Also, the WW3 wave energy is not as broadly distributed in terms of direction as in the MR measurement. The MR and WW3 spectra in Fig. 12b show two distinct

wave systems, with the dominant one being swell from the east. WW3 registered higher frequency energy for this system which is not present in the MR record. Nevertheless, the two spectra agree remarkably well. This is especially noteworthy in view of the zero-pixel percentage of 46 %, which indicates the presence of rain (Lund et al. 2012). Figure 12c shows wave energy from three systems, spreading over all directions. The dominant system according to the MR spectral partitioning comes from the east, whereas the peak WW3 system comes from the south. This is likely due to a mismatch between the U_{10N} measured on the ship

(~13 m s^{-1} from east-northeast) and the one forcing the WW3 waves (off by ~2 m s^{-1} and ~20°). Figure 12d, e shows pairs of wave spectra that are ~19 h apart. The earlier pair shows four prominent wave systems. Again, the energetic order of the secondary and tertiary WW3 system is reversed compared with the MR results. Both spectra have their most energetic system in wind direction, however, neither peak is forced by the wind (i.e., the above wind sea criteria are not met). In the later pair of spectra (Fig. 12e), two swells merged into a single system. The previously dominant system lost energy, and a southwestern swell gained energy, claiming the top rank in WW3. Finally, Fig. 12f shows spectra with a single dominant wind sea system from the north-northeast. The MR recorded an additional wave system of negligible energy from the south. Side-by-side comparisons of 2D wave spectra are inherently qualitative and subjective. The examples shown here span over the full study period and are representative of the larger data set. This assertion is strengthened by the excellent MR–WW3 agreement in terms of mean direction and directional spreading as function of frequency (see Section 4.2).

5 Discussion and conclusions

This study uses WW3 wave modeling results to help establish MR's strength at monitoring multi-directional seas. It may be argued that comparing MR and WW3 results cannot be considered a proper validation of either product. This is why the model was first validated against EASI buoy measurements. A comparison with in situ measurements would indeed be desirable, but the MR was the only wave sensor on the *Revelle*, and times during which the ship was in the vicinity of either EASI buoy were few and far between (Collins et al. 2014). On the other hand, the fact that the model delivers 2D wave spectra is an argument that favors the use of WW3 results over in situ point measurements.

The standard MR wave retrieval method (Young et al. 1985; Senet et al. 2001; Nieto Borge et al. 2004) has been improved in several ways. Several of these improvements represent adaptations of a recently developed near-surface vertical current shear measurement technique to wave retrieval (Lund et al. 2015b). The wave analysis is performed over the whole radar FOV to minimize the range and azimuth dependency, the dispersion filter's Doppler shift is defined as a function of wavenumber to account for near-surface vertical current shear, and the background noise is utilized to better distinguish signal from noise. To ensure accurate shipboard MR results, the backscatter data are georeferenced using auxiliary heading and GPS measurements. Given sufficiently accurate auxiliary data, this and other improvements guarantee underway shipboard wave measurements of a quality that is comparable with results from coastal MR stations (e.g., Nieto Borge and Guedes Soares 2000). This assertion stands in contrast to the notion of Stredulinsky and Thornhill (2011) and Cifuentes-Lorenzen et al. (2013) that shipboard MR wave results can only be conditionally trusted.

Compared with EASI, the MR–WW3 comparison gave higher correlation coefficients and lower standard deviations for all spectral wave parameters except H_s. The MR directional spreading and mean wave direction show excellent qualitative agreement with WW3. Interestingly, both MR and WW3 results suggest that, on average, the directional spreading decreases at the very low frequencies. This can be interpreted as evidence that the increased low-frequency directional spreading reported by EASI is due to measurement noise. Using spectral partitioning techniques, it was furthermore demonstrated that MR and WW3 accurately measure and predict multimodal seas. On a couple occasions, both measurements and model reported the presence of four simultaneous wave systems. Numerous simultaneous wave systems could be tracked over extended time periods.

The study results suggest that MR accurately reproduces the multi-directional wave field. By providing fully directional wave spectra, MRs can be a valuable complement or even alternative to standard wave buoy measurements. Moreover, to these authors' knowledge, MR is the only sensor capable of measuring 2D wave spectra from an underway vessel. The results also highlight WW3's skill at predicting swell-dominated seas. Note that due to the relative difficulty of modeling swell, Rogers and Wang (2007) performed their validation of directional wave predictions in Lake Michigan, where wind seas predominate.

The MR wave retrieval is still hindered by an incomplete understanding of the grazing incidence X-band backscatter mechanisms. Additional work is needed to improve the MTF that transforms MR image into wave spectra. Further improvements can be expected from utilizing a vertically polarized antenna (Huang and Gill 2012). Also, the H_s calibration becomes unnecessary if H_s is derived from the wave crest-induced shadowing in the MR images instead of the SNR (Gangeskar 2014). In the future, coherent MRs may be used to retrieve 2D wave spectra without empirical transfer function, by measuring the waves' orbital motion (Trizna 2012).

References

Al-Habashneh AA, Moloney C, Gill EW, Huang W (2015) An adaptive method of wave spectrum estimation using X-band nautical radar. Remote Sens 7(12):15851. doi:10.3390/rs71215851. http://www.mdpi.com/2072-4292/7/12/15851

Alpers WR, Ross DB, Rufenach CL (1981) On the detectability of ocean surface waves by real and synthetic aperture radar. J Geophys Res 86(C7):6481–6498. doi:10.1029/JC086iC07p06481

Barrick DE (1968) A review of scattering from surfaces with different roughness scales. Radio Sci 3:865–868

Bell PS, Osler JC (2011) Mapping bathymetry using X-band marine radar data recorded from a moving vessel. Ocean Dyn 61(12):2141–2156. doi:10.1007/s10236-011-0478-4

Capon J, Greenfield RJ, Kolker RJ (1967) Multidimensional maximum-likelihood processing of a large aperture seismic array. Proc IEEE 55(2):192–211

Cifuentes-Lorenzen A, Edson JB, Zappa CJ, Bariteau L (2013) A multisensor comparison of ocean wave frequency spectra from a research vessel during the Southern Ocean Gas Exchange Experiment. J Atmos Oceanic Technol 30(12):2907–2925. doi:10.1175/JTECH-D-12-00181.1

Collins CO III, Lund B, Ramos RJ, Drennan WM, Graber HC (2014) Wave measurement intercomparison and platform evaluation during the ITOP (2010) experiment. J Atmos Oceanic Technol 31(10):2309–2329

D'Asaro E, Black P, Centurioni L, Chang YT, Chen S, Foster RC, Graber H, Harr P, Hormann V, Lien RC, Lin II, Sanford T, Tang TY, Wu CC (2014) Impact of typhoons on the ocean in the Pacific: ITOP. Bull Am Meteor Soc 95(9):1405–1418. doi:10.1175/BAMS-D-12-00104.1

Dittmer J (1995) Use of marine radars for real time wave field survey and speeding up transmission/processing. In: Proceedings of WMO/IOC workshop on operational ocean monitoring using surface based radars, vol 32. World Meteorological Organization, Geneva, pp 133–137

Donelan MA, Hamilton J, Hui WH (1985) Directional spectra of wind-generated waves. Philos Trans R Soc Lond Ser A Math Phys Sci 315(1534):509–562

Drennan WM, Graber HC, Collins CO III, Herrera A, Potter H, Ramos RJ, Williams NJ (2014) EASI: an air–sea interaction buoy for high winds. J Atmos Oceanic Technol 31(6):1397–1409. doi:10.1175/JTECH-D-13-00201.1

Ewans KC (1998) Observations of the directional spectrum of fetch-limited waves. J Phys Oceanogr 28(3):495–512. doi:10.1175/1520-0485(1998)028<0495:OOTDSO>2.0.CO;2

Firing E, Hummon JM (2010) Shipboard ADCP measurements. The GO-SHIP repeat hydrography manual: a collection of expert reports and guidelines IOCCP report ICPO Publication Series Number 134(14):1–11

Gangeskar R (2014) An algorithm for estimation of wave height from shadowing in X-band radar sea surface images. IEEE Trans Geosci Remote Sens 52(6):3373–3381

Graber HC, Terray EA, Donelan MA, Drennan WM, Van Leer JC, Peters DB (2000) ASIS—a new air–sea interaction spar buoy: design and performance at sea. J Atmos Oceanic Technol 17(5):708–720. doi:10.1175/1520-0426(2000)017<0708:AANASI>2.0.CO;2

Hanson JL, Phillips OM (2001) Automated analysis of ocean surface directional wave spectra. J Atmos Oceanic Technol 18(2):277–293. doi:10.1175/1520-0426(2001)018<0277:AAOOSD>2.0.CO;2

Hasselmann S, Hasselmann K, Allender JH, Barnett TP (1985) Computations and parameterizations of the nonlinear energy transfer in a gravity-wave specturm. Part II: parameterizations of the nonlinear energy transfer for application in wave models. J Phys Oceanogr 15(11):1378–1391. doi:10.1175/1520-0485(1985)015<1378:CAPOTN>2.0.CO;2

Hessner KG, Nieto-Borge JC, Bell PS (2008) Nautical radar measurements in Europe: applications of WaMoS II as a sensor for sea state, current and bathymetry. In: Remote sensing of the European seas. Springer, pp 435–446

Holthuijsen LH, Powell MD, Pietrzak JD (2012) Wind and waves in extreme hurricanes. J Geophys Res 117(C9). doi:10.1029/2012JC007983, C09003

Huang W, Gill E (2012) Surface current measurement under low sea state using dual polarized X-band nautical radar. IEEE J Sel Topics Appl Earth Observ 5(6):1868–1873. doi:10.1109/JSTARS.2012.2208179

IOC, IHO, BODC (2003) Centenary edition of the GEBCO Digital Atlas, published on CD-ROM on behalf of the Intergovernmental Oceanographic Commission and the International Hydrographic Organization as part of the General Bathymetric Chart of the Oceans. British Oceanographic Data Centre, Liverpool

Izquierdo P, Guedes Soares C, Nieto Borge JC, Rodríguez Rodríquez G (2004) A comparison of sea-state parameters from nautical radar images and buoy data. Ocean Eng 31(17–18):2209–2225. http://www.sciencedirect.com/science/article/pii/S0029801804000988

Khandekar ML, Lalbeharry R, Cardone V (1994) The performance of the canadian spectral ocean wave model (CSOWM) during the grand banks ERS-1 SAR wave spectra validation experiment. Atmos-Ocean 32(1):31–60. doi:10.1080/07055900.1994.9649489

Krogstad HE, Wolf J, Thompson SP, Wyatt LR (1999) Methods for intercomparison of wave measurements. Coastal Eng 37(3–4):235–257. doi:10.1016/S0378-3839(99)00028-9. http://www.sciencedirect.com/science/article/pii/S0378383999000289

Kuik AJ, van Vledder GP, Holthuijsen LH (1988) A method for the routine analysis of pitch-and-roll buoy wave data. J Phys Oceanogr 18(7):1020–1034. doi:10.1175/1520-0485(1988)018<1020:AMFTRA>2.0.CO;2

Longuet-Higgins MS, Cartwright D, Smith N (1963) Observations of the directional spectrum of sea waves using the motions of a floating buoy. Ocean Wave Spectra. Prentice-Hall, Easton, pp 111–136

Ludeno G, Orlandi A, Lugni C, Brandini C, Soldovieri F, Serafino F (2014) X-band marine radar system for high-speed navigation purposes: a test case on a cruise ship. IEEE Geosci Remote Sens 11(1):244–248

Lund B, Graber HC, Romeiser R (2012) Wind retrieval from shipborne nautical X-band radar data. IEEE Trans Geosci Remote Sens 50(10):3800–3811. doi:10.1109/TGRS.2012.2186457

Lund B, Collins CO III, Graber HC, Terrill E, Herbers THC (2014) Marine radar ocean wave retrieval's dependency on range and azimuth. Ocean Dynam 64(7):999–1018. doi:10.1007/s10236-014-0725-6

Lund B, Graber HC, Hessner K, Williams NJ (2015a) On shipboard marine X-band radar near-surface current "calibration". J Atmos Oceanic Technol 32(10):1928–1944. doi:10.1175/JTECH-D-14-00175.1

Lund B, Graber HC, Tamura H, Collins CO III, Varlamov SM (2015b) A new technique for the retrieval of near-surface vertical current shear from marine X-band radar images. J Geophys Res C: Oceans. doi:10.1002/2015JC010961

Lygre A, Krogstad HE (1986) Maximum entropy estimation of the directional distribution in ocean wave spectra. J Phys Oceanogr 16(12):2052–2060. doi:10.1175/1520-0485(1986)016<2052:MEEOTD>2.0.CO;2

Lyzenga DR, Ericson EA (1998) Numerical calculations of radar scattering from sharply peaked ocean waves. IEEE Trans Geosci Remote Sens 36(2):636–646

Nieto Borge JC, Guedes Soares C (2000) Analysis of directional wave fields using X-band navigation radar. Coastal Eng 40(4):375–391

Nieto Borge JC, Reichert K, Dittmer J (1999) Use of nautical radar as a wave monitoring instrument. Coastal Eng 37(3–4):331–342

Nieto Borge JC, Rodríquez Rodríguez G, Hessner K, Izquierdo González P (2004) Inversion of marine radar images for surface wave analysis. J Atmos Oceanic Technol 21(8):1291–1300

Nieto Borge JC, Hessner K, Jarabo-Amores P, de la Mata-Moya D (2008) Signal-to-noise ratio analysis to estimate ocean wave heights from X-band marine radar image time series. IET Radar Sonar Navig 2(1):35–41

Plant WJ (2003) Microwave sea return at moderate to high incidence angles. Wave Random Media 13(4):339–354. doi:10.1088/0959-7174/13/4/009

Potter H, Graber HC, Williams NJ, Collins CO III, Ramos RJ, Drennan WM (2015) In situ measurements of momentum fluxes in typhoons. J Atmos Sci 72(1):104–118. doi:10.1175/JAS-D-14-0025.1

Rogers WE, Wang DWC (2006) On the validation of directional wave prediction: review and discussion. Tech. rep., NRL/MR17320-06-8970, 40pp

Rogers WE, Wang DWC (2007) Directional validation of wave predictions. J Atmos Oceanic Technol 24(3):504–520. doi:10.1175/JTECH1990.1

Saha S, Moorthi S, Pan HL, Wu X, Wang J, Nadiga S, Tripp P, Kistler R, Woollen J, Behringer D et al (2010) The NCEP climate forecast system reanalysis. Bull Am Meteor Soc 91(8):1015–1057

Senet CM, Seemann J, Ziemer F (2001) The near-surface current velocity determined from image sequences of the sea surface. IEEE Trans Geosci Remote Sens 39(3):492–505

Stewart RH, Joy JW (1974) HF radio measurements of surface currents. Deep-Sea Res Oceanogr Abstr 21(12):1039–1049

Stredulinsky DC, Thornhill EM (2011) Ship motion and wave radar data fusion for shipboard wave measurement. J Ship Res 55(2):73–85

Tamura H, Waseda T, Miyazawa Y (2009) Freakish sea state and swell-windsea coupling: numerical study of the Suwa-Maru incident. Geophys Res Lett 36(1):L01607. doi:10.1029/2008GL036280

Teng CC (2002) Wave measurements from NDBC buoys and C-MAN stations, vol 1. OCEANS '02 MTS/IEEE, pp 517–524

Tolman HL (2009) User manual and system documentation of WAVE-WATCH III version 3.14. Technical note, MMAB Contribution, NCEP, Camp Springs, MD (276)

Tolman HL, Chalikov D (1996) Source terms in a third-generation wind wave model. J Phys Oceanogr 26(11):2497–2518

Trizna DB (2012) Coherent marine radar measurements of directional wave spectra using vertically polarized antennas. Oceans 2012:1–5. doi:10.1109/OCEANS.2012.6404904

Trizna DB, Hansen JP, Hwang P, Wu J (1991) Laboratory studies of radar sea spikes at low grazing angles. J Geophys Res 96(C7):12529–12537

Wetzel LB (1990) Surface waves and fluxes. Kluwer, Dordrecht, chap Electromagnetic scattering from the sea at low grazing angles, pp 109–171

Wyatt LR, Green JJ, Gurgel KW, Nieto Borge JC, Reichert K, Hessner K, Günther H, Rosenthal W, Saetra O, Reistad M (2003) Validation and intercomparisons of wave measurements and models during the EuroROSE experiments. Coastal Eng 48(1):1–28. http://www.sciencedirect.com/science/article/pii/S0378383902001576

Young IR, Rosenthal W, Ziemer F (1985) A three-dimensional analysis of marine radar images for the determination of ocean wave directionality and surface currents. J Geophys Res 90(C1):1049–1059

Ziemer F (1995) An instrument for the survey of the directionality of the ocean wave field. In: Proceedings of WMO/IOC workshop on operational ocean monitoring using surface based radars, vol 32, pp 81–87

Ziemer F, Dittmer J (1994) A system to monitor ocean wave fields, vol 2. In: Proc. Oceans. IEEE, pp 28–31